Cross-sectional analysis of lithium ion electrodes using spatial autocorrelation techniques†

Michael J. Lain, [ID] *[ab] Geanina Apachitei, [ID] [ab] Luis Román-Ramírez, [ID] [abc] Mark Copley [ID] [ab] and James Marco[ab]

Join counting, a standard technique in spatial autocorrelation analysis, has been used to quantify the clustering of carbon, fluorine and sodium in cross-sectioned anode and cathode samples. The sample preparation and EDS mapping steps are sufficiently fast for every coating from two Design of Experiment (DoE) test matrices to be characterised. The results show two types of heterogeneity in material distribution; gradients across the coating from the current collector to the surface, and clustering. In the cathode samples, the carbon is more clustered than the fluorine, implying that the conductive carbon component is less well distributed than the binder. The results are correlated with input parameters systematically varied in the DoE *e.g.* coating blade gap, coating speed, and other output parameters *e.g.* coat weight, and electrochemical resistance.

Introduction

To operate successfully, lithium ion batteries need to utilise all the active materials that are present in the composite electrodes; across the entire X–Y plane, and in the Z direction from metal current collectors to the polymeric separator. To achieve this requires careful process control during the mixing, coating and calendering stages of electrode production,[1,2] along with sound design of the electrode formulations.[3] In the Z direction, the active material particles need electronic conduction to the current collectors, and ionic conduction in the electrolyte filled pores. At high rates of charge and discharge, one of these conduction pathways often becomes rate limiting, particularly for thicker electrodes. However, performance can also be limited by sub-optimal electrode manufacturing. Some examples of process control failures and their consequences are collected in Table 1.[4–15]

The Nextrode project, funded by the Faraday Institution, is exploring various aspects of lithium ion cell manufacture. It is intended to be complementary to the Dalion projects at Braunschweig University,[16] the Artistic project at the Université de Picardie Jules Verne,[17] and the European Defacto project.[18] One part of the Nextrode project is using a Design of Experiments (DoE) approach to investigate electrode manufacturing.[19–21]

Typically, a single mix is coated using different control parameters like blade gap and coating speed. The electrodes are then characterised (coat weight, thickness, adhesion), and tested in coin cells. The electrochemical performance is the most important evaluation criterion, but other physical parameters are also informative.

There is an increasing mathematical understanding of the processes than can occur during the solvent drying stage of coating, based on the dimensionless Peclet (P_e) numbers for evaporation and sedimentation.[10–12] Initially, the particles of active material tend to sediment, and the coating shrinks to a minimum thickness. However, the binder and conductive carbon are still mobile in the remaining solvent, and their final distribution depends on the relative rates of diffusion and evaporation. A high evaporation rate moves the smaller particles to the surface of the coating, while a high diffusion rate gives a uniform particle distribution. The Peclet numbers for evaporation and sedimentation are defined as:

$$P_e \text{ (evap)} = \text{Evap. rate} \times \text{Initial film thickness}/D \qquad (1)$$

$$P_e \text{ (sed)} = \text{Particle radius} \times \text{Settling rate}/D \qquad (2)$$

If $P_e \gg 1$, then either evaporation or sedimentation are favoured over diffusion. If P_e (evap) and P_e (sed) are both $\gg 1$, then the preferential process can be estimated from the ratio of the particle settling rate to the solvent evaporation rate.[12]

The Stokes Einstein coefficient for particle diffusion $D = kT/6\Pi\mu r$, where μ is the solvent viscosity and r is the particle radius. The settling speed for a single particle is $U = 2r^2g(\rho_s - \rho_f)/9\mu$, where ρ_s and ρ_f are the densities of the solid particles and surrounding fluid, respectively. Introducing these terms into the P_e definition equations

[a] WMG, University of Warwick, Coventry, CV4 7AL, UK.
E-mail: m.j.lain@warwick.ac.uk
[b] The Faraday Institution, UK
[c] School of Engineering, London South Bank University, London SE1 0AA, UK

This journal is © the Owner Societies 2022

Phys. Chem. Chem. Phys., 2022, **24**, 29999–30009 | **29999**

Table 1 Process control failures during electrode manufacturing

Process	Control failure	Consequence	Ref.
Mixing	Incomplete de-agglomeration	Streaky coatings	4
Mixing	Incomplete carbon de-agglomeration	Poor rate performance	5–7
Mixing	Settling of components	Variations along coat length	4
Mixing	Shortening of polymeric binder chains	Poor coating adhesion	8
Coating	Solvent evaporation too fast	Cracking of coating, craters	9
Coating	Solvent evaporation too slow	Phase separation	10–12
Coating	Blockages in slurry feed lines	Streaks, non-uniform coating	13
Calendering	Calendering temperature too high	Skin of binder on surface	14, 15
Calendering	Calendering pressure too high	Cracking of active particles	14, 15

gives P_e (evap) $\propto r$ and P_e (sed) $\propto r^4$, so the nano-sized conductive carbon particles are very unlikely to sediment. As the solvent continues to evaporate, the assumptions of dilute solution theory become increasingly less valid.[10] Eventually, the binder concentration will exceed the solubility limit in the coating solvent, and solid binder will precipitate.

In this paper, we investigate a technique based on the mathematical field of spatial autocorrelation. The coatings are cross-sectioned for examination by scanning electron microscopy (SEM), and the elements are mapped using energy dispersive X-ray spectroscopy (EDS). The anodes contain a carboxy methyl cellulose (CMC) binder, which is partially substituted with sodium. The distribution of the binder can therefore be mapped by the sodium. Similarly, in cathodes, the poly vinylidene difluoride (PVDF) binder can be mapped using fluorine. Cathodes also contain carbon, as part of the PVDF, and as a conductivity enhancing agent. Electrodes are often classified into regions of active material, binder + conductive carbon, and pores.[1,22] Therefore, these elements are not expected to be homogeneously distributed throughout the anodes and cathodes. However, if the carbon is more clustered than the fluorine, then the implication is that the conductive carbon is not as well dispersed as the PVDF binder. This could be due to incomplete de-agglomeration of the carbon during mixing, or from phase separation during drying, or both. Intuitively, the rate performance of the electrode will be better with fully dispersed carbon. Spatial autocorrelation is a method of quantifying the degree of clustering, for each element.

The concepts of spatial autocorrelation are illustrated by the patterns shown in Fig. 1. For the halved distribution of white and grey squares, there is clearly a great deal of correlation. For the chequerboard pattern, there is ordering but not clustering. The random distribution is disordered, but there is some clustering. Quantification of spatial autocorrelation typically uses techniques like Moran's I Index[23] and Geary's G ratio.[24]

Join counting is a simplified version of spatial autocorrelation, ideal when there is a regular grid pattern, and a binary 0 or 1 value.[25] The number of adjacent 0–0, 0–1 and 1–1 squares is counted, and compared to the mean and standard deviation for a random distribution, to give a Z score of statistical significance:

$$\text{Joins(one−one)} = 0.5 \times \sum_i \sum_j x_i \cdot x_j \tag{3}$$

$$Z_{1-1} \frac{(\text{Observed} - \text{Expected})}{\text{Standard Deviation}} \tag{4}$$

The expected (mean) and standard deviation values have to be measured for a random distribution with the same surface coverage as the experimental sample e.g. 50% in the patterns in Fig. 1. When squares have a range of values rather than a binary 0 or 1, the Moran I Score can be calculated using:

$$\text{Moran I Score} = \frac{N}{\sum w_{ij}} \cdot \frac{\sum_i \sum_j w_{ij} \cdot (x_i - \bar{x}) \cdot (x_j - \bar{x})}{\sum_i (x_i - \bar{x})^2} \tag{5}$$

In this equation, $\bar{x}$ is the mean of the variable of interest x, N is the number of spatial units, and w_{ij} is a matrix of weightings. Typically w_{ij} is 1 if the units are adjacent, and 0 otherwise. The Moran I Score is a value between 0 and 1, with 0 for no correlation, and 1 for perfect correlation.
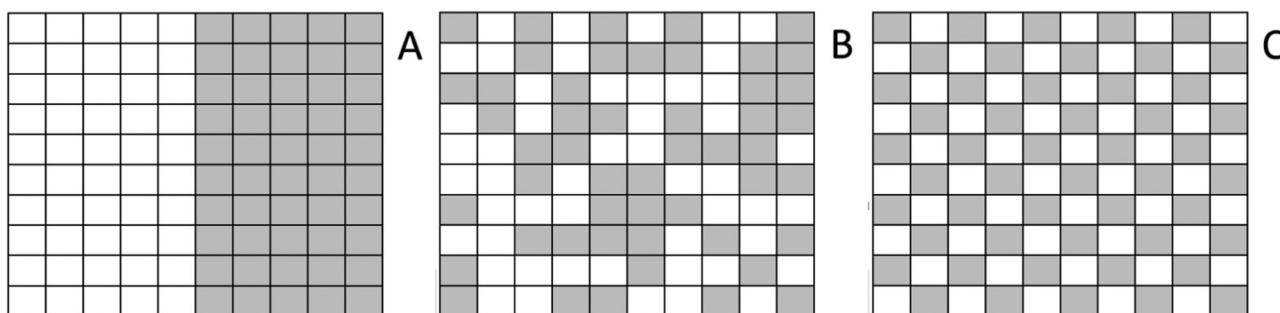

Fig. 1 Examples of patterns with different degrees of spatial autocorrelation. (A) Halved, (B) Random and (C) Chequer board.

A similar approach to join counting has been used to quantify binder homogeneity.[4] The local binder volume fraction in each square of a 50×50 grid was compared with the overall binder volume fraction in the coating, and summed to create a binder homogeneity index. The experimental data used in the analysis was an EDS fluorine map from an X–Y image for a NCA:PVDF:AB = 85.6:8:6.4 wt% cathode coating[26] (NCA = $LiNi_{0.8}Co_{0.15}Al_{0.05}O_2$ and AB = acetylene black). The homogeneity was then modelled for different mixing protocols, using active materials with different shapes and particles sizes.[4] NCA:PVDF:CB = 94:3:3 wt% coatings were prepared with solids contents in the range 57–70% (CB = carbon black), and the planar EDS fluorine maps were analysed, along with other properties like mix viscosity.[27] Visually, the PVDF was most uniformly distributed for a solids content of around 64%, with more clustering at the extremes of the solids content range.

The carbon and manganese distributions in an NMC-111:PVDF:carbon black = 95:2.5:2.5 wt% cathode were correlated with the electrochemical performance, for different drying temperatures and shear rates.[28] The EDS spectra were processed to include only the highest intensity pixels, representing the surface elemental layer. 2D radial distribution functions were then calculated for carbon–carbon and carbon–manganese pixels. The best rate performance was obtained for coatings with both short range and long range ordering of the carbon–manganese distribution. The carbon–carbon correlations were less significant, with similar radial distribution functions for electrodes with high and low rate performance. Cross-sectional EDS maps of carbon and fluorine were measured during an investigation of the effect of calendering temperature on NMC-111 cathodes.[29] Visually, there was more clustering of both carbon and fluorine for a 94:3:3 mix than for a 90:5:5 mix, and more clustering of carbon then fluorine in both mixes.

EDS measurements have also been made on graphite:PVDF:C65 = 92:5.2:2.8 wt% coatings, in both X–Y planar and cross-sectional modes, to study the influence of drying temperature.[30] To measure the fluorine content at the interface between the coating and the copper foil, the copper foil was peeled off, with the coating taped to a sample holder. As the drying temperature increased from 65 °C to 90 °C, the fluorine content at the surface increased from 4.3 wt% to 5.6 wt%, and at the interface decreased from 4.9 wt% to 3.8 wt%. Cross-sectional EDS measurements were used to create a "false colour" map of fluorine content, with clear evidence of clustering. To achieve a sufficiently good signal to noise ratio, each spectrum took 8.5 hours to record.

A similar approach was used to measure the fluorine distribution in graphite:PVDF = 95:5 coatings.[31] The relatively thick coatings were peeled off the copper current collector, and potted in epoxy resin between two aluminium plates. Cross sectional SEM/EDS images were obtained after polishing with SiC paper (coarse and fine), and then with a diamond solution applied to a micro cloth. For drying temperatures of 25–50 °C, the fluorine gradient was minimal, whereas for 100–125 °C, the fluorine content at the surface was at least ten times the value at the current collector.

The fluorine distribution across graphite:PVDF:carbon black = 91:6:3 wt% coatings was measured using EDS, as part of a wider investigation of anode formulation and drying conditions.[32] The measurements used polished cross sectional samples, and the EDS measurements were validated with laser-induced breakdown spectroscopy (LIBS). There was a gradient of fluorine concentrations across the coating, with higher values near the surface. The gradient increased with the amount of energy (J cm^{-2}) added during the drying process.

To differentiate between graphite and conductive carbon, anodes were prepared using 25 nm carbon coated iron particles.[33] The coatings were graphite:PVDF:Fe–C = 95:2.5:2.5, and deliberately prepared in homogeneous and heterogeneous versions, by changing the drying temperature profile. In the homogeneous coating, the fluorine and iron had similar distributions, whereas in the heterogeneous coating, both elements showed more clustering. Integration of the elemental intensities showed lower iron and fluorine contents at the current collector of the homogeneous coating. However, for the heterogeneous coating, the iron was roughly uniform from top to bottom, while the fluorine content showed a threefold increase from current collector to surface.

There is increasing knowledge about conductive carbon phase distributions in lithium ion coating slurries. Particle size distribution measurements show both permanently bound aggregates, with a particle size of around 0.2 μm, and agglomerates, with a particle size of around 3 μm.[34] Electrochemical, spectroscopic and simulation results were combined to consider various possible distributions of the carbon–binder domain.[35] The electrochemical measurements on an NMC-622:PVDF:SFG6L:Super P$^{®}$ = 94:3:1:2 were full discharge tests at different rates, and impedance measurements in symmetrical cells. Electrodes were examined using SEM/EDS, and X-ray tomography was used to reconstruct the structure of the active material particles. The modelling then used three different CBD distributions; randomly within the pore structure, coated on the surface of the active particles, or concentrated at the close contact points between the particles of the active material. The contact point model gave the best fit to the experimental data, and appeared the closest physical match to the SEM images. The CBD was modelled as 1 μm particles, even though the SFG6L graphite has a D_{50} of 3.5 μm, and Super P$^{®}$ carbon black has a nominal particle size of 0.04 μm.

The influence of electrode formulation and mixing protocol on the carbon black distribution has recently been characterised using mercury porosimetry.[36] The pores in the carbon black phase are much smaller than the pores between the NMC particles. A lower porosity value for the carbon black phase implied greater dispersion i.e. deagglomeration or fragmentation. There was an optimum porosity to minimise the coating resistance, and maximise the 5 C:0.1 C capacity ratio.

The redistribution of electrode components during drying has been simulated using a 3D model,[37] based on a slurry containing NMC-111:PVDF:CB = 94:3:3 in NMP. The carbon binder domain (CBD) was modelled as discrete particles, with diameters of 5.7 μm when solvated, and 1.3 μm when dry. Migration of the CBD particles occurred in the second part of the drying process, after sedimentation of the active material particles. The amount of migration increased with faster drying rates.

This journal is © the Owner Societies 2022

Phys. Chem. Chem. Phys., 2022, 24, 29999–30009 | 30001

The Design Of Experiments approach has been applied to various parts of lithium ion cell development, from the synthesis of new active materials to the understanding of lifetime ageing processes, *via* the optimisation of electrode formulations. The application of the DoE approach to diverse energy applications has been reviewed,[38] including an introduction to response surface methodology. Response surface optimisation was used in the preparation of $LiFePO_4/C$ active materials, by a carbothermal reduction method.[39] Similarly, the Taguchi method was used in the synthesis of copper doped $LiFePO_4/C$, with a co-precipitation method.[40] A DoE approach has recently been applied to electrode formulations involving LFP ($LiFePO_4$) cathodes and LTO ($Li_4Ti_5O_{12}$) anodes.[41] An orthogonal design of experiments was used to investigate capacity fade in NCA/graphite 18 650 cells.[42]

This paper describes the use of join counting on EDS elemental maps from cross-sectioned anodes and cathodes, produced as part of two DoE test matrices. The data was also integrated to plot the gradients of carbon and fluorine or sodium, in the Z direction. The results are correlated with the control parameters in the coating process, and also other output parameters from physical and electrochemical measurements. For the cathode coatings, measurements were made on both uncalendered and calendered samples. The former are compared with the coating conditions, and the latter with the cell test results. It is also possible to look at changes to the electrode structure during calendering.

Experimental

The electrode coatings were prepared using a one litre Eirich mixer, and coated using a Megtec coater with three drying zones. The anode mix formulation was BTR S-360 E-3 graphite : BVH8 CMC : BM-451B SBR : Imerys C45 = 95.25 : 1.5 : 2.25 : 1.0 wt% (SBR = styrene butadiene rubber). The cathode mix was NMC-622 : Solef® 5130 : Imerys C65 = 96 : 2 : 2 wt%. The coatings used 10 μm copper and 15 μm aluminium foils, respectively. During the coatings, all the control parameters were kept constant, except those being systematically changed as part of the DoE. The blade gap and speed of the metal foil are well known parameters. In a reverse comma bar configuration, the coating ratio (CR) is the relative rotational speed of the transfer and bumper bar rollers, within a recommended range of 100–150%. In normal operation, the blade gap and coating ratio are adjusted to achieve the target coat weight. In these experiments, the two values were set, and the coat weight was allowed to vary.

After drying, all the electrodes were calendered to their target porosity of 30 ± 1%, using an Innovative Machine Corporation calender. Electrode disks were cut, and used to prepare coin cell half cells, in an argon filled glove box. The separator was Celgard® H1609, and the electrolyte was 1 mol dm^{-3} $LiPF_6$ in EC : EMC = 3 : 7, with 1 wt% VC (EC = ethylene carbonate, EMC = ethyl methyl carbonate and VC = vinylene carbonate). The coin cells were tested using BioLogic

BCS-805 units, in an air conditioned laboratory at 25 °C. The test protocol included a slow formation cycle at ± C/20, five conditioning cycles, rate tests at up to 10 C (discharge or delithiation), and ASI resistance measurements at nine states of charge (ASI = area specific resistance[43]). The ASI tests involved 1.8 C discharge pulses and 1.2 C charge pulses, both with a ten second duration. For each cell, the values were averaged over the range where the ASI was independent of the state of charge (typically 30–90% SoC). Ideally, the values for the three equivalent cells for each coating would have been averaged. However, given the variability in the values, it was decided to select the minimum value from the three cells.

Pieces of each coating were also characterised using SEM/EDS. Discs of coating were cross-sectioned using a Bright microtome, and then mounted vertically on metal tags, using conductive carbon tape. The samples were then analysed using a Hitachi TM3030 desktop SEM, fitted with an Oxford Instruments EDS (30 mm^2 detection area). Typically, the area of coating mapped was around 125 × 75 μm. This produced an EDS map containing around 250 × 110 pixels. Three different approaches were used to perform spatial autocorrelation measurements on the EDS maps, as shown schematically in Fig. 2. Each pixel in the EDS map has a value between 0 (black) and 255 (white). For join counting, it is necessary to define a threshold to convert this to a 0 or 1 value. For the processed images with maximum contrast (❶), the threshold was around 125. The surface coverage (proportion of white squares) was relatively insensitive to the threshold value. For unprocessed images (❷), the threshold was lower, and could be varied to change the surface coverage value.

However, the main benefit of using the whole image was in defining the precise coating region. It was difficult to determine the edge of the coating from the EDS image, particularly if the sample was not perfectly vertical during the measurement. The best approach to defining the edge was from measurements on the higher resolution SEM image. The join counting calculation requires a mean and standard deviation value, for a random distribution with the same surface coverage as the sample. This was obtained using ten iterations of the RAND() function in Excel, with a 250 × 100 grid.

Results and discussion

Cathode DoE

An initial scoping DoE used five input or control variables, each with two levels. The DoE described here used only three inputs (blade gap, coating ratio and coating speed), but with five different levels. This produced a test matrix of twenty coatings, as set out in a table in the ESI.† The resulting images for one of these coatings are shown in Fig. 3. For each EDS map, the Z_{1-1} value and Moran I Score was calculated, using the methods ❷ and ❸ in Fig. 2. The ESI† contains a table of the join counting values, and plots of carbon and fluorine concentrations across the coatings.
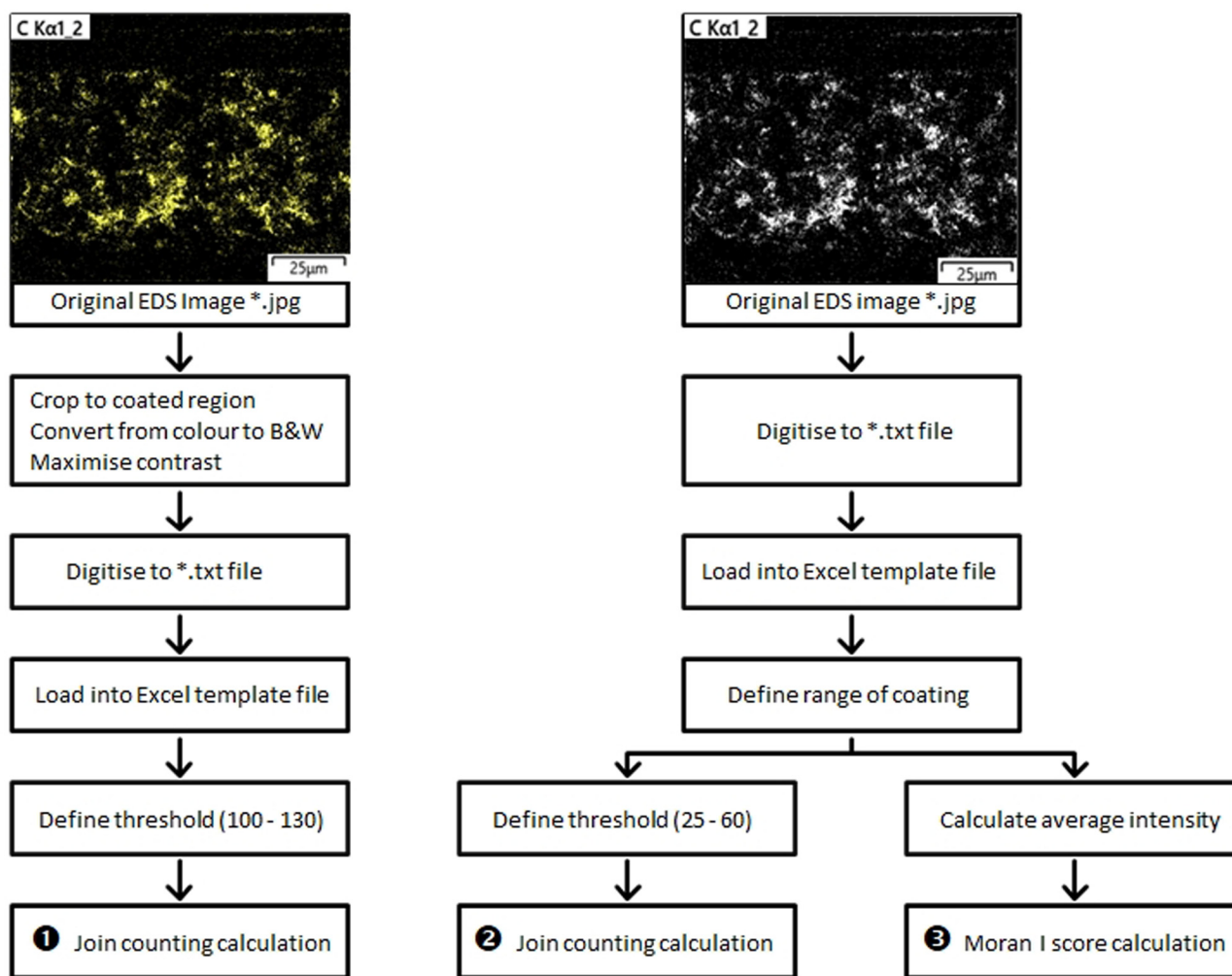
30002 | *Phys. Chem. Chem. Phys.*, 2022, **24**, 29999–30009

This journal is © the Owner Societies 2022

Fig. 2 Alternative options for EDS data analysis.

As already mentioned, uncalendered coatings are the best representation of the electrode structure after coating. Some correlations arising from the EDS analysis are plotted in Fig. 4. The Z_{1-1} values were not dependent on input parameters like blade gap and coating speed, or output parameters like coat weight. However, the carbon values were consistently higher than for fluorine. This implies more clustering of the carbon, and hence the conductive carbon used in the electrode mix.

The most important tests in the DoE are for electrochemical performance, which necessitates the use of calendered electrode pieces. Fig. 5 compares the spatial autocorrelation results with two results from coin cell tests. Resistances (ASI) were measured using short, ten second pulses, and full discharge capacities were measured at different rates. The carbon Z_{1-1} score increased with increased resistance, and to some extent with the 5 C : 0.2 C capacity ratio.
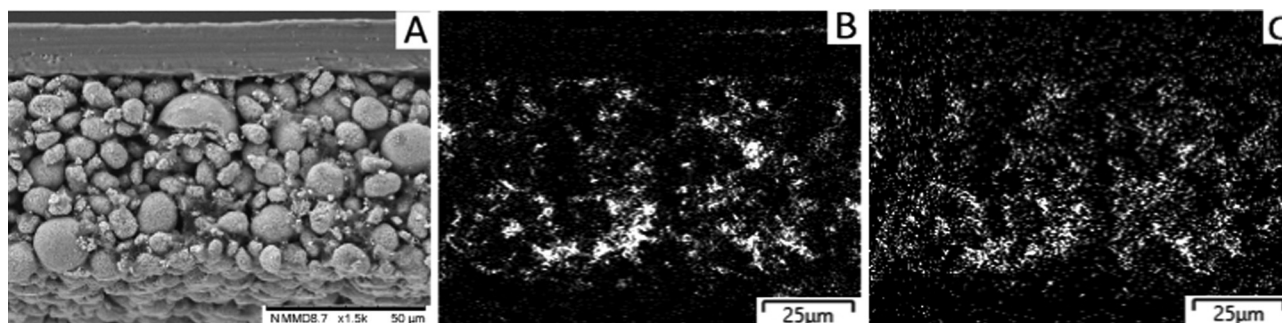

Fig. 3 Typical images from cathode DoE. (A) SEM Image, (B) EDS Map For C 1 s, and (C) EDS Map For F 1s.

This journal is © the Owner Societies 2022

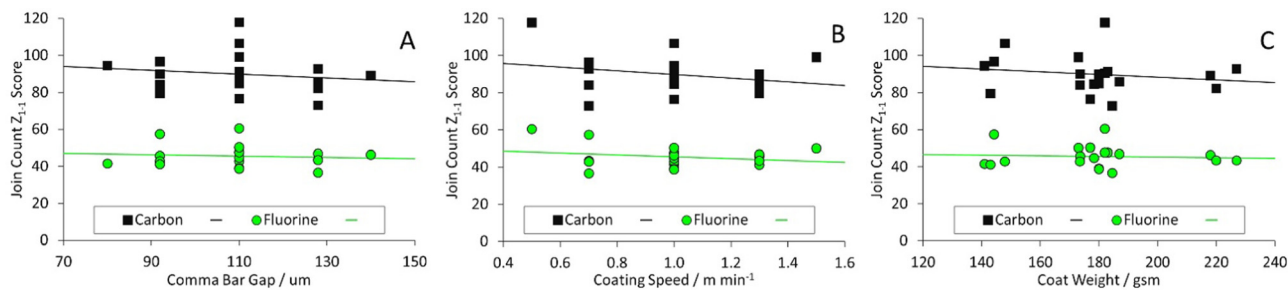*Phys. Chem. Chem. Phys.*, 2022, **24**, 29999–30009 | **30003**

Fig. 4 Analysis of results from cathode DoE (uncalendered samples). (A) Z_{1-1} vs. blade gap, (B) Z_{1-1} vs. coating speed, and (C) Z_{1-1} vs. coat weight.

The ASI is mainly dependent on the intrinsic resistivity of the electrode, whereas the discharge capacity at 5 C also depends on mass transport within the electrode structure. In consequence, the 5 C : 0.2 C capacity ratio is strongly dependent on the coating thickness, with thicker coatings giving much lower ratios. However, according to ASI theory,[43] the ASI is inversely proportional to the coating thickness. This leads to very high ASI values for very thin coatings, but all the coatings tested here were in the region where the change of ASI with thickness is relatively gentle. The Moran I scores for carbon also increased with resistance, along with the fluorine values.

One benefit of using a microtome rather than FIB (focused ion beam) to cross-section samples is that the characterisation area is several millimetres long. This enables a representative section of the coating to be selected for analysis, and repeat measurements along the sample length. Even so, the measured area is a microscopic fraction of the total coating. Duplicate measurements allow any anomalous readings to be excluded. The DoE test matrix also included a number of deliberate repeats, as part of the statistical validation process. There is a table of calculated mean and standard deviation values for these sample types in the ESI.† For most of the Z_{1-1} join counting and Moran I scores, the standard deviations were less than 10% of the mean values. The exception was the results for the carbon measurements on the calendered electrode samples. The twenty samples were analysed in two batches of ten, on different days, as with the uncalendered samples. However, for the calendered samples, the response of the spectrometer changed between batches.

Calendering can potentially change the degree of clustering of both the binder and the conductive carbon in the electrode.

To investigate this, Fig. 6 compares the join counting and Moran I scores before and after calendering, for both carbon and fluorine. The guide lines in these graphs are for equality, rather than a linear regression fitting. Therefore, points below the line represent a decrease in clustering after calendering. This occurred for more than half of the carbon measurements, and most of the fluorine values. Fig. 6(C) compares the fluorine and carbon Moran I scores for the calendered and uncalendered coatings, this time with linear regression lines. There was reasonably good correlation within each data set. A proportion of the carbon EDS signal comes from the PVDF binder, and the carbon and binder are expected to be associated in their own domain within the electrode structure.

The EDS images can also be analysed to obtain plots of the carbon and fluorine proportions across the electrode, from the aluminium foil to the surface. The results for all the coatings are collected in the ESI.† To remove the fluctuations, Fig. 7 plots the gradients fitted using linear regression. Some of the uncalendered coatings showed surface depletion of carbon and/or fluorine, following a maximum at around 80% of the total thickness.

However, in most cases the surface concentration of both elements was higher than the value at the current collector. In several cases there was an excess of carbon at the surface, and often the carbon gradient at the surface increased after calendering. Generally, the carbon gradients were steeper than the fluorine gradients. However, the correlation between the gradients before and after calendering was poor, for both elements.

An increase in fluorine content from current collector to coating surface has been consistently observed in previous
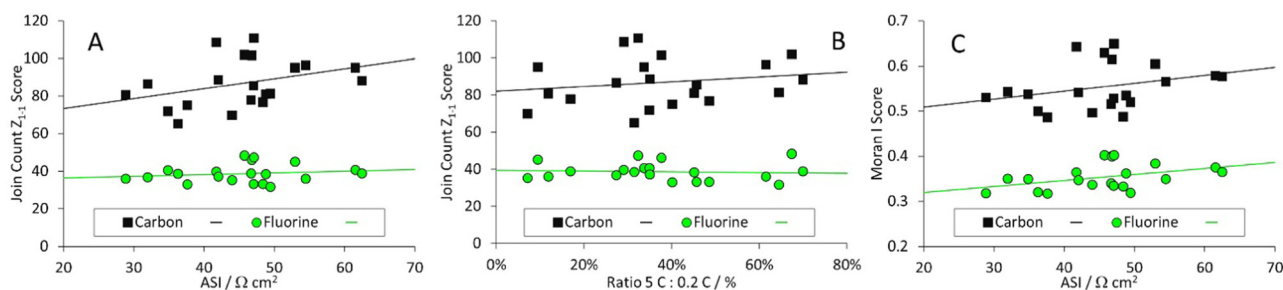

Fig. 5 Analysis of results from cathode DoE (calendered samples). (A) Z_{1-1} vs. resistance (ASI), (B) Z_{1-1} vs. rate performance, and (C) Moran I score vs. ASI resistance.

30004 | Phys. Chem. Chem. Phys., 2022, 24, 29999–30009

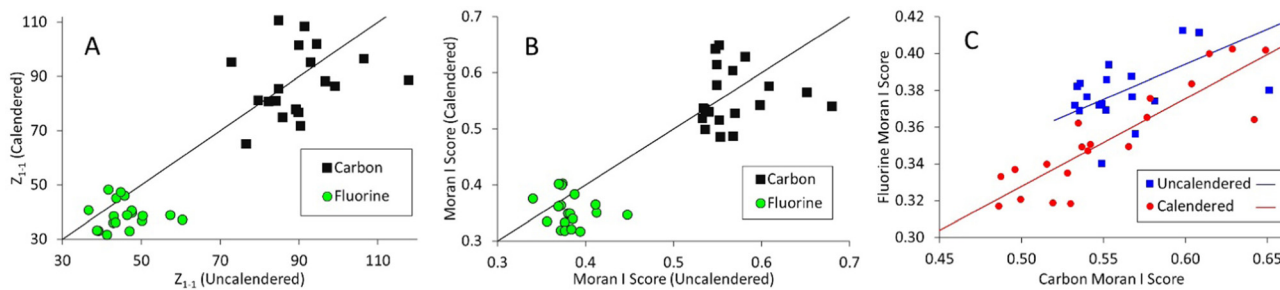This journal is © the Owner Societies 2022

Fig. 6   Effect of calendering on clustering. (A) Z_{1-1} values, (B) Moran I scores, and (C) fluorine vs. carbon Moran I scores.
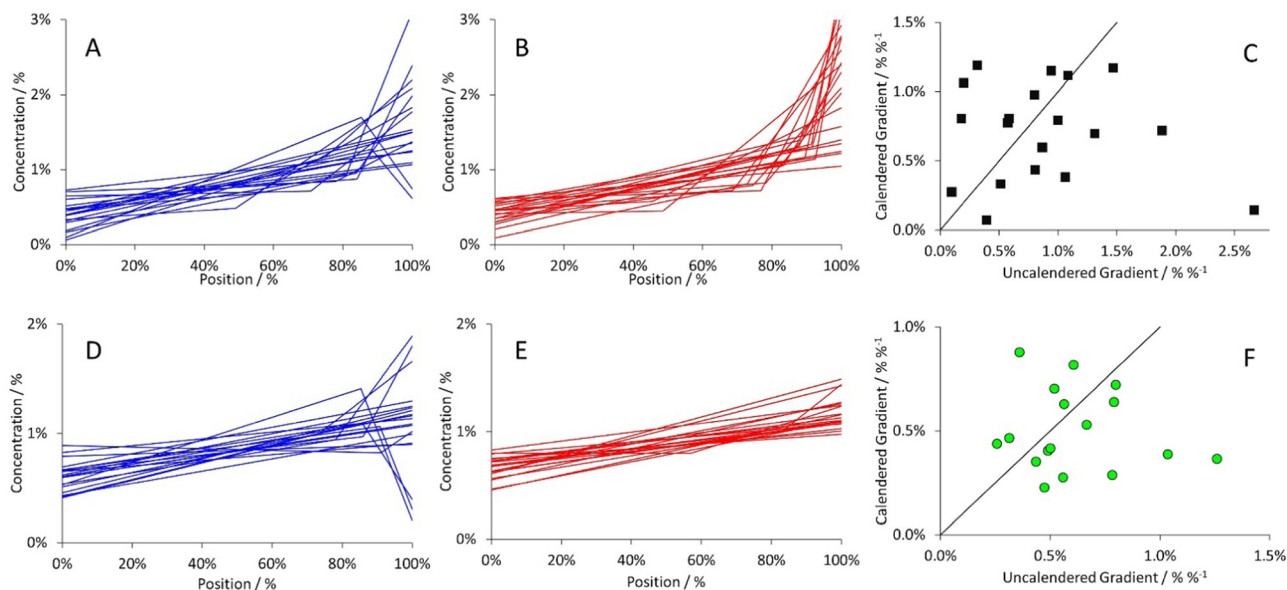

Fig. 7   Analysis of carbon and fluorine gradients from cathode DoE. (A) Carbon (uncalendered), (B) carbon (calendered), (C) carbon (calendered vs. uncalendered), (D) fluorine (uncalendered), (E) fluorine (calendered), and (F) fluorine (calendered vs. uncalendered).

experimental studies,[30–33] and predicted in modelling work.[36] More clustering of carbon than fluorine was also reported previously, with a similar cathode mix.[29] The Peclet number for evaporation is around 5000 for conductive carbon in an NMP/PVDF mix at 100 °C. The calculation is shown in the ESI.† Since $P_e \gg 1$, evaporation is favoured over diffusion, an increased surface concentration of carbon is likely. The effective particle size for PVDF molecules is calculated to be similar to the conductive carbon, so an increased fluorine content towards the surface is also expected. Moreover, in the same way that carbon black particles can agglomerate, polymer chains in solution can entangle into larger entities,[44] with an increased effective particle size and hence P_e.

The P_e evaporation number is proportional to the initial film thickness, and also the ratio of the evaporation rate to the absolute temperature. However, there was no correlation between the carbon or fluorine gradients and the coating thickness, or with the other input parameters. With such a large P_e number, it may be difficult to identify more subtle effects. Overall, the drying process involves complicated

interactions between all the control parameters. Given this complexity, it was easier to find correlations with output parameters, rather than input parameters. The area specific impedance (ASI) was measured using relatively short current pulses. Less clustering of the conductive carbon should lead to a lower resistance, and indeed this was the case. The complexities in the drying process are discussed in greater detail, later in this document.

An interesting observation was that in many cases, calendering increased the amount of carbon in the surface layer of the electrode. Another observation was that in calendered coatings, some of the clumps of conductive carbon were below the surface defined by the active material particles (see SEM/EDS images in ESI†). Two mechanisms that could explain this are illustrated in Fig. 8. In the non-uniform calendering option (A → B), the particles of active material near the surface move more than those near the metal foil. Since the carbon is bonded to the active material particles, this increases the local concentration of carbon. An alternative explanation is that as the conductive carbon and binder particles move towards the
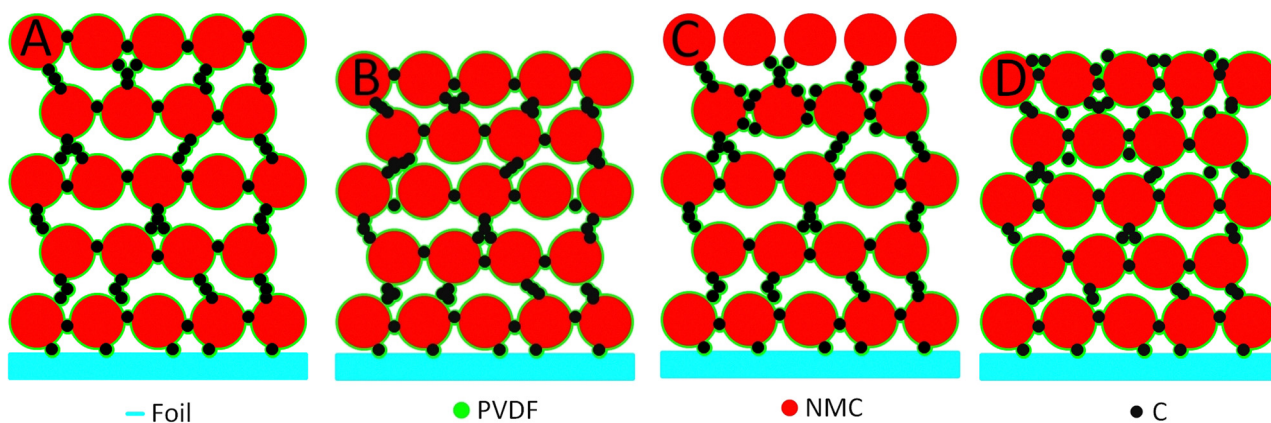
This journal is © the Owner Societies 2022

Phys. Chem. Chem. Phys., 2022, 24, 29999–30009 | 30005

Fig. 8 Possible mechanisms for increased surface carbon content after calendering. (A) Original coating, (B) non-uniform calendering, (C) original coating (carbon maximum) (D) push through.

surface, the solvent in the surface region has already evaporated. This creates a local maximum in the carbon and fluorine concentrations below the surface (some plots in Fig. 7(A) and (D)). During calendering, the active material particles push through this carbon–binder domain, again increasing the surface carbon content (C → D). Both mechanisms should also increase the surface fluorine content, which was not observed experimentally. However, if more of the binder is attached to the active material particles than the carbon clusters, then push through would increase the surface carbon more than the surface fluorine. It is possible that both mechanisms occur at the same time. In a 3D modelling study,[37] there was more compaction and less resulting porosity in the upper layer of the coating *i.e.* the non-uniform calendering model. However, the model did not include the influence of temperature on the deformation properties of the different components.

Anode DoE

The anode DoE used two control variables with five possible levels, leading to thirteen combinations. The variables were the blade gap and coating ratio; the coating speed was kept constant at 1.0 m min^{-1}. The DoE matrix is set out in the ESI,† along with detailed results for each coating. Fig. 9 shows a typical SEM of a cross-sectioned coating, along with EDS maps for carbon and sodium. There is a near overlap of the Na K-α

and Cu L-α peaks (1.041 keV *vs.* 0.929 keV), which causes some sodium to be detected in the region of the copper foil.

As with the cathode DoE, the EDS images were used to calculate join count Z_{1-1} values and Moran I scores, for the sodium. Unfortunately, it is not possible to differentiate between the graphite active material and the conductive carbon additive using EDS. There was no obvious correlation between these values and either of the input parameters. The results of various attempted correlations with other output parameters are plotted in Fig. 10. The Z_{1-1} scores for sodium were mostly around 40, similar to the values fluorine in the calendered cathode samples. The Moran I scores were around 0.285 for sodium and 0.350 for fluorine. This suggests slightly less clustering of the NaCMC binder in the anode than the PVDF binder in the cathode.

Unfortunately, there was no obvious correlation between the spatial autocorrelation measurements and any of the input or other output parameters. There was a mixture of positive, zero and negative gradients across the coatings. Overall, there was no correlation between gradient and coat weight, and the gradients were less than for the fluorine in the cathode samples. The graphs show calculated linear regression lines, but the *y* axes were relatively sensitive, and the human eye would probably have drawn a horizontal line.

The effective size of the CMC "particles" is calculated to be similar to the PVDF "particles". However, the P_e number for
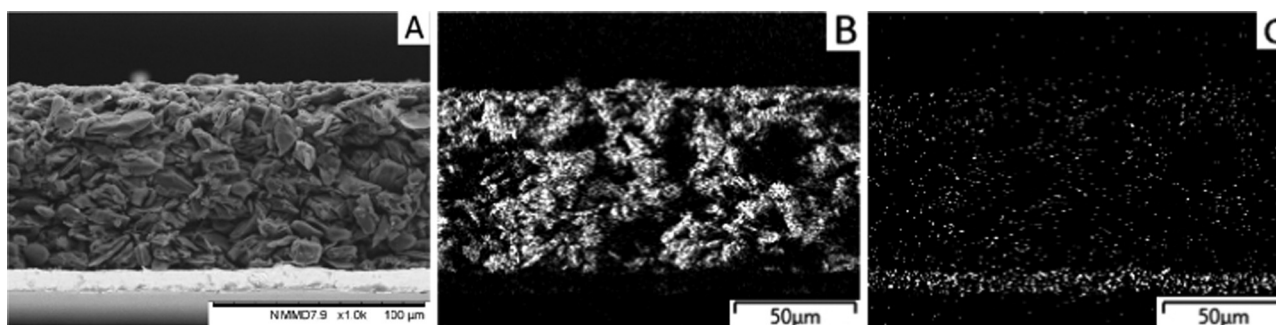

Fig. 9 Typical results from anode DoE. (A) SEM image, (B) EDS map for C 1s, and (C) EDS map for Na 1s.

30006 | *Phys. Chem. Chem. Phys.*, 2022, **24**, 29999–30009

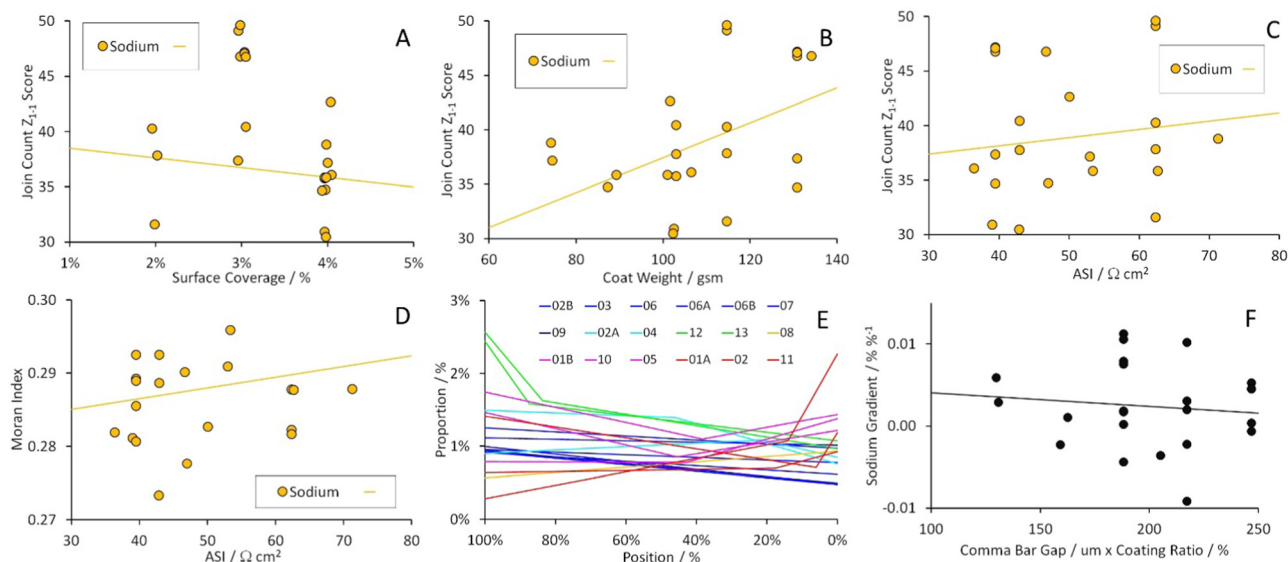This journal is © the Owner Societies 2022

Fig. 10 Analysis of results from anode DoE. (A) Z_{1-1} vs. surface coverage, (B) Z_{1-1} vs. coat weight, (C) Z_{1-1} vs. ASI resistance, (D) Moran I Score vs. ASI resistance, (E) sodium gradient, and (F) sodium gradient vs. coat weight.

conductive carbon in water/CMC at 30 °C is estimated to be less than 10. Therefore, it would not be surprising if there was less movement of the CMC under evaporation, compared to PVDF. This would lead to less clustering, and less steep gradients, as observed experimentally. The electrochemical resistance and rate performance did not depend on the binder distribution, as found with the PVDF binder in the cathode coatings.

As with the cathode samples, repeat measurements were made on some coatings, and there were duplicate tests built into the DoE matrix. The mean and standard deviations for these samples are tabulated in the ESI.† For the join counting Z_{1-1} scores, the standard deviations were around 10% of the mean values. For the Moran I Scores, the standard deviations were less than 0.010.

Simple coating model

To investigate the lack of correlation with any of the individual input parameters, a simple iterative model for film thickness in

a coater with three heating zones was prepared. Fig. 11(A) shows calculated values for film thickness with three different initial film thicknesses (μm), and three different coating speeds (m min^{-1}). The activation energy for the evaporation rate was based on, ref. 10 but the actual rates were significantly faster (dedicated coater, rather than drying oven). Fig. 11(B) shows the key transition point, from sedimentation of the active material particles to evaporation of the remaining solvent. During this stage, the binder and conductive carbon are still mobile. The relative rates of evaporation and diffusion will determine whether the distribution remains uniform, or the particles migrate towards the surface. It is evident from Fig. 11(B) that the temperature profiles beyond the nine transition points are different. P_e (evap) $\propto \mu/T$, and the viscosity μ will change as the concentration of binder in the liquid phase increases. As already noted, the validity of dilute solution theory at this point must be questionable.[10]

The spatial autocorrelation measurements have shown that the electrochemical performance of the cathode depends on
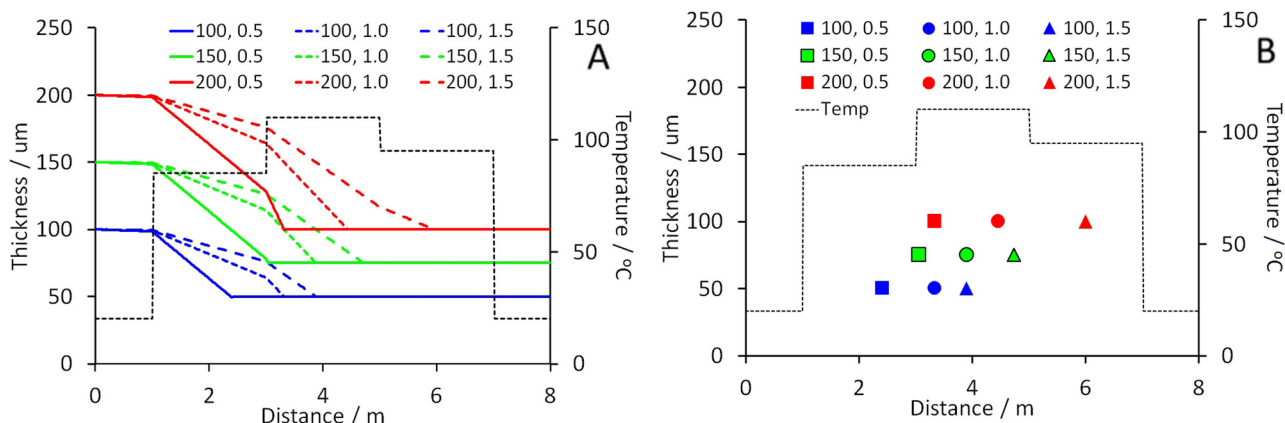

Fig. 11 Modelling of coating thickness during drying. (A) Coating thickness, and (B) transition point from sedimentation to evaporation.

the morphology of the electrode, and particularly the distribution of the conductive carbon. In turn, this depends on the prevailing conditions during the evaporation stage of the coating process. A simple 3×3 matrix of input conditions gave seven different thermal profiles during the evaporation stage. All electrochemical tests use calendered electrodes, and calendering can change the electrode structure, over and above the reduction in porosity. Thus, it is very unlikely that the electrochemical performance will show strong correlation with any single input parameter to the coating process.

Conclusions

The use of spatial autocorrelation methods gives an invaluable insight into the structure of the binder + conductive carbon phase, in lithium ion electrodes. This is very difficult to achieve using complementary techniques like X-ray tomography. Using a microtome rather than FIB to cross-section the electrodes allowed every coating in two DoEs to be analysed, and the opportunity to select representative and/or multiple regions for characterisation.

The main results from the spatial autocorrelation measurements are:

– An increase in carbon clustering corresponds to an increase in resistance in electrochemical tests.

– The carbon is more clustered than the fluorine in cathode coatings.

– The fluorine (PVDF) in cathodes shows similar clustering to the sodium (NaCMC) in anodes.

– There is a gradient in the carbon and fluorine concentrations from the metal foil to the coating surface.

– On average, the sodium gradients are effectively zero.

– There is no correlation between the spatial autocorrelation measurements and any of the individual input values to the coating process, as part of the DoE.

– The carbon–binder domain is not homogeneous within the electrode structure.

– The carbon and binder components can (and do) have different distributions.

– The carbon and binder distributions can (and do) change during calendering.

– Before calendering, carbon particles may accumulate just below the surface, rather than at the surface.

– Uncalendered coatings should be used to investigate variations in the coating process, but calendered coatings need to be used for comparison with electrochemical cell performance.

The results can be (partially) interpreted by consideration of the Peclet evaporation numbers for the two coatings. These are ~ 5000 for NMP/PVDF and <10 for water/CMC, so steeper concentration gradients would be expected for carbon and fluorine than sodium. The most likely cause of the higher degree of carbon clustering in the cathodes is a failure to fully de-agglomerate the carbon particles during mixing, though re-agglomeration could occur during coating and drying. This

will be considered further in a DoE investigating mixing protocols.

Author contributions

Conceptualisation – all, methodology – LARR, investigation – MJL, GA, formal analysis – MJL, writing (original draft) – MJL, writing (review & editing) – MC, JM.

Conflicts of interest

There are no conflicts to declare.

Acknowledgements

Notes and references

1 H. Bockholt, M. Indrikova, A. Netz, F. Golks and A. Kwade, *J. Power Sources*, 2016, **325**, 140.

2 J. Li, J. Fleetwood, W. B. Hawley and W. Kays, *Chem. Rev.*, 2021, **122**, 903.

3 H. Zheng, R. Yang, G. Liu, X. Song and V. S. Battaglia, *J. Phys. Chem. C*, 2012, **116**, 4875.

4 A. Kraytsberg and Y. Ein-Eli, *Adv. Energy Mater.*, 2016, **6**, 1600655.

5 Z. Liu, V. Battaglia and P. P. Mukherjee, *Langmuir*, 2014, **30**, 15102.

6 Z. Liu and P. P. Mukherjee, *J. Electrochem. Soc.*, 2014, **161**, E3248.

7 M. Wang, D. Dang, A. Meyer, R. Arsenault and Y.-T. Cheng, *J. Electrochem. Soc.*, 2020, **167**, 100518.

8 S. Byun, J. Choi, Y. Roh, D. Song, M.-H. Ryou and Y. M. Lee, *Electrochim. Acta*, 2020, **332**, 135471.

9 Z. Du, K. M. Rollag, J. Li, S. J. An, M. Wood, Y. Sheng, P. P. Mukherjee, C. Daniel and D. L. Wood III, *J. Power Sources*, 2017, **354**, 200.

10 M. Stein, A. Mistry and P. P. Mukherjee, *J. Electrochem. Soc.*, 2017, **164**, A1616.

11 S. Jaiser, L. Funk, M. Baunach, P. Scharfer and W. Schabel, *J. Colloid Interface Sci.*, 2017, **494**, 022.

12 S. Baesch, K. Price, P. Scharfer, L. Francis and W. Schabel, *Chem. Eng. Process.*, 2018, **123**, 138.

13 L. David, R. E. Ruther, D. Mohanty, H. M. Meyer III, Y. Sheng, S. Kalnaus, C. Daniel and D. L. Wood III, *Appl. Energy*, 2018, **231**, 446.

14 C. Meyer, H. Bockholt, W. Haselrieder and A. Kwade, *J. Mater. Process. Technol.*, 2017, **249**, 172.

15 T. Günther, D. Schreiner, A. Metkar, C. Meyer, A. Kwade and G. Reinhart, *Energy Technol.*, 2020, **8**, 1900026.

16 **https://www.tu-braunschweig.de/iwf/fup/mofa/forschung sprojekte/dalion40**.

30008 | *Phys. Chem. Chem. Phys.*, 2022, **24**, 29999–30009

This journal is © the Owner Societies 2022

17 https://www.erc-artistic.eu/.

18 https://www.defacto-project.eu/.

19 L. A. Román-Ramírez, G. Apachitei, M. Faraji-Niri, M. J. Lain, W. D. Widanage and J. Marco, *J. Power Sources*, 2021, **516**, 230689.

20 L. A. Román-Ramírez, G. Apachitei, M. Faraji-Nin, M. J. Lain, D. Widanage and J. Marco, *Int. J. Energy Environ. Sci.*, 2022, s40095-022-00481-w.

21 L. A. Román-Ramírez, G. Apachitei, M. Faraji Niri, M. J. Lain, D. Widanage and J. Marco, *Data Brief*, 2022, **40**, 107720.

22 A. C. Ngandjong, T. Lombardo, E. N. Primo, M. Chouchane, A. Shodiev, O. Arcelus and A. A. Franco, *J. Power Sources*, 2021, **485**, 229320.

23 P. A. P. Moran, *Biometrika*, 1950, **37**, 17.

24 R. C. Geary, *The Incorporated Statistician*, 1954, vol. 5, p. 115, 129.

25 A. D. Cliff and K. Ord, *Economic Geography*, 1970, vol. 46, p.269.

26 G. Liu, H. Zheng, X. Song and V. S. Battaglia, *J. Electrochem. Soc.*, 2012, **159**, A214.

27 L. Ouyang, Z. Wu, J. Wang, X. Qi, Q. Li, J. Wang and S. Lu, *RSC Adv.*, 2020, **10**, 19360.

28 R. M. Saraka, S. L. Morelly, M. H. Tang and N. J. Alvarez, *ACS Appl. Energy Mater.*, 2020, **3**, 11681.

29 C. Meyer, M. Weyhe, W. Haselrieder and A. Kwade, *Energy Technol.*, 2020, **8**, 1900175.

30 M. Müller, L. Pfaffmann, S. Jaiser, M. Baunach, V. Trouillet, F. Scheiba, P. Scharfer, W. Schabel and W. Bauer, *J. Power Sources*, 2017, **340**, 1.

31 R. Morasch, J. Landesfeind, B. Suthar and H. A. Gasteiger, *J. Electrochem. Soc.*, 2018, **165**, A3459.

32 B. G. Westphal and A. Kwade, *J. Energy Storage*, 2018, **18**, 509.

33 S. L. Morelly, J. Gelb, F. Iacoviello, P. R. Shearing, S. J. Harris, N. J. Alvarez and M. H. Tang, *ACS Appl. Energy Mater.*, 2018, **1**, 4479.

34 J. K. Mayer, L. Almar, E. Asylbekov, W. Haselrieder, A. Kwade, A. Weber and H. Nirschl, *Energy Technol.*, 2020, **8**, 1900161.

35 S. Hein, T. Danner, D. Westhoff, B. Prifling, R. Scurtu, L. Kremer, A. Hoffmann, A. Hilger, M. Osenberg, I. Manke, M. Wohlfahrt-Mehrens, V. Schmidt and A. Latz, *J. Electrochem. Soc.*, 2020, **167**, 013546.

36 J. K. Mayer, H. Bockholt and A. Kwade, *J. Power Sources*, 2022, **529**, 231259.

37 T. Lombardo, A. C. Ngandjong, A. Belhcen and A. A. Franco, *Energy Storage Mater.*, 2021, **43**, 337.

38 L. A. Román-Ramírez and J. Marco, *Appl. Energy*, 2022, **320**, 119305.

39 K. Yang, F. Tan, F. Wang, Y. Long and Y. Wen, *Chin. J. Chem. Eng.*, 2012, **20**, 793.

40 H.-C. Liu, Y.-M. Wang and C.-C. Hsieh, *Ceram. Int.*, 2017, **43**, 3196.

41 O. Rynne, M. Dubarry, C. Molson, E. Nicolas, D. Lepage, A. Prébé, D. Aymé-Perrot, D. Rochefort and M. Dollé, *ACS Appl. Energy Mater.*, 2020, **3**, 2935.

42 L. Su, J. Zhang, C. Wang, Y. Zhang, Z. Li, Y. Song, T. Jin and Z. Ma, *Appl. Energy*, 2016, **163**, 201.

43 K. G. Gallagher, P. A. Nelson and D. W. Dees, *J. Power Sources*, 2011, **196**, 2289.

44 A. Korolkovas, P. Gutfreund and J.-L. Barrat, *J. Chem. Phys.*, 2016, **145**, 124113.

This journal is © the Owner Societies 2022

Phys. Chem. Chem. Phys., 2022, **24**, 29999–30009 | **30009**